# Two-photon spectroscopy of mercury and velocity-selective double resonances

Thomas Beyer, Daniel Kolbe,* Martin Scheid, Frank Markert, and Jochen Walz
*Institut für Physik, Johannes Gutenberg-Universität Mainz, Staudinger Weg 7, D-55128 Mainz, Germany*
(Received 27 August 2009; published 12 November 2009)

Two-photon laser spectroscopy of the $6\,^1S_0-7\,^1S_0$ transition in mercury has been performed using two copropagating continuous-wave laser beams. One laser beam is at 254 nm wavelength and can be tuned to the $6\,^1S_0-6\,^3P_1$ resonance. The other laser beam is at 408 nm. Two very different regimes can be distinguished, one far off resonance and one near resonance with the one-photon resonance. A resonance which is not Doppler broadened has been observed for low Rabi frequencies. This velocity-selective double resonance in a three-level ladder system is analogous to the dark resonance in three-level $\Lambda$ systems.

DOI: 10.1103/PhysRevA.80.053414 PACS number(s): 32.80.Wr, 32.80.Qk, 31.15.xg

## I. INTRODUCTION

Two-photon laser spectroscopy is a powerful tool which has several applications. Time-resolved two-photon spectroscopy has been used for precise measurements of lifetimes in mercury [1]. The linear Doppler effect can be suppressed using counterpropagating beams and great precision can be achieved [2]. Furthermore, in three-level or multiple-level systems several quantum effects can be observed. Suppressed two-photon absorption due to destructive interference of multiple excitation passes has been observed [3]. Resonant coupling of two levels can result in electromagnetic-induced transparency suppressing the one-photon excitation [4]. In $\Lambda$ systems coupling of the two lower levels by a two-photon resonance results in a dark resonance of the upper level [5,6].

A two-photon transition can also be used to enhance the nonlinear susceptibility in four-wave mixing schemes [7]. Using such a scheme we are developing a next-generation high-power Lyman-$\alpha$ source at 121.56 nm wavelength which is based on two-photon enhanced four-wave mixing of laser beams at 254, 408, and 546 nm wavelengths in mercury vapor [8]. Details on the laser systems at 254 and 546 nm can be found in [9,10]. The wavelengths of the 254 and 408 nm beams are adjusted to match the exact two-photon resonance $6\,^1S_0-7\,^1S_0$ in mercury.

In this paper, we present a detailed investigation of this two-photon resonance in a three-level ladder system. For small detunings, one-photon resonance and two-photon resonance are competing processes. For low Rabi frequencies, a non-Doppler-broadened resonance appears, the velocity-selective double resonance. It is analogous to the dark resonance in three-level $\Lambda$ systems [5,6].

Section II of this paper discusses the calculation of line shapes and the origin of the velocity-selective double resonance is explained. The experimental setup is discussed in Sec. III. Section IV presents the experimental results and compares them with calculations.

## II. CALCULATION OF LINE SHAPES

The relevant part of the mercury level scheme is a three-level system in a ladder configuration, which is shown in Fig. 1. The levels are connected by two laser fields at 254 and 408 nm. We consider excitation energies very close to the atomic transition energies (detunings of 100 GHz down to a few GHz). Contributions from other off-resonant energy levels can thus be neglected. We use the semiclassical approach of Brewer and Hahn [11], but we take the wave vectors of the exciting laser fields to be parallel. In the density-matrix formalism, the appropriate optical Bloch equations are

$$\dot{\rho}_{11} = i\alpha(\tilde{\rho}_{31} - \tilde{\rho}_{13}) + \Gamma_{31}\rho_{33} + \Gamma_{21}\rho_{22}, \tag{1a}$$

$$\dot{\rho}_{33} = i\alpha(\tilde{\rho}_{13} - \tilde{\rho}_{31}) + i\beta(\tilde{\rho}_{23} - \tilde{\rho}_{32}) + \Gamma_{23}\rho_{22} - \Gamma_{31}\rho_{33}, \tag{1b}$$

$$\dot{\rho}_{22} = i\beta(\tilde{\rho}_{32} - \tilde{\rho}_{23}) - (\Gamma_{21} + \Gamma_{23})\rho_{22}, \tag{1c}$$

$$\dot{\tilde{\rho}}_{13} = i\alpha(\rho_{33} - \rho_{11}) - i\beta\tilde{\rho}_{12} - (i\delta_{13} + \gamma_{31})\tilde{\rho}_{13}, \tag{1d}$$

$$\dot{\tilde{\rho}}_{23} = i\beta(\rho_{33} - \rho_{22}) - i\alpha\tilde{\rho}_{21} + (i\delta_{23} - \gamma_{23})\tilde{\rho}_{23}, \tag{1e}$$

$$\dot{\tilde{\rho}}_{12} = i\alpha\tilde{\rho}_{32} - i\beta\tilde{\rho}_{13} - [i(\delta_{13} + \delta_{23}) + \gamma_{21}]\tilde{\rho}_{12}. \tag{1f}$$

The diagonal elements $\rho_{ii}$ describe the populations in level $|i\rangle$ (with $i=1,2,3$) and the off-diagonal elements $\tilde{\rho}_{ij}$ (with $i \neq j$) represent the coherences between levels $|i\rangle$ and $|j\rangle$. The detunings of the incident laser fields to the transition energies are $\delta_{13}$ and $\delta_{23}$. $\alpha$ and $\beta$ are the corresponding Rabi frequencies.

The difference between the optical Bloch equations in Eqs. (24a)–(24f) of Ref. [11] and the ones described above is the definition of the decay rates, which is crucial for both diagonal and off-diagonal density-matrix elements. We define the decay rate $\Gamma_{ij}$ for the population decay of level $|i\rangle$ to level $|j\rangle$. For mercury, the decay rates have the following values: the intermediate level $6\,^3P_1$ has a lifetime of $\tau_3 = 122$ ns $= \Gamma_{31}^{-1}$ [12] and only decays into the ground state $6\,^1S_0$. The upper level $7\,^1S_0$ has a lifetime of $\tau_2 = 32.1$ ns $= (\Gamma_{21}+\Gamma_{23})^{-1}$ and decays with a branching ratio of 13.0% into $6\,^3P_1$ (given by $\Gamma_{23}$) and 87.0% into $6\,^1P_1$ [13]. The $6\,^1P_1$ state decays into $6\,^1S_0$ and has a lifetime of 1.48 ns [14], which is very short compared to the $7\,^1S_0-6\,^1P_1$ decay. Hence, we can neglect this decay and denote the decay rate

*kolbed@uni-mainz.de

 

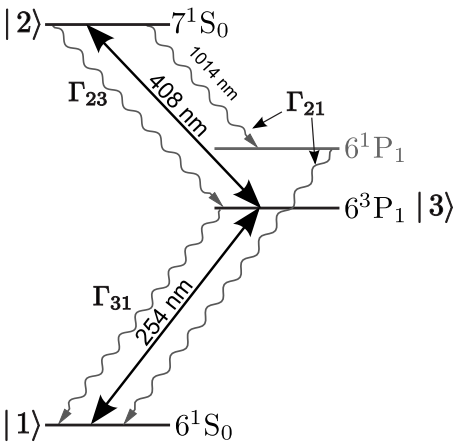


FIG. 1. Simplified level scheme of mercury. The laser fields at 254 nm and 408 nm wavelengths couple to the $6\ ^1S_0-6\ ^3P_1$ and $6\ ^3P_1-7\ ^1S_0$ transitions, respectively. The detunings of the laser fields to the corresponding transition energies are $\delta_{13}$ and $\delta_{23}$. The fluorescence at 1014 nm due to the decay of the $7\ ^1S_0$ state into the $6\ ^1P_1$ state is proportional to the population in the $7\ ^1S_0$ state.

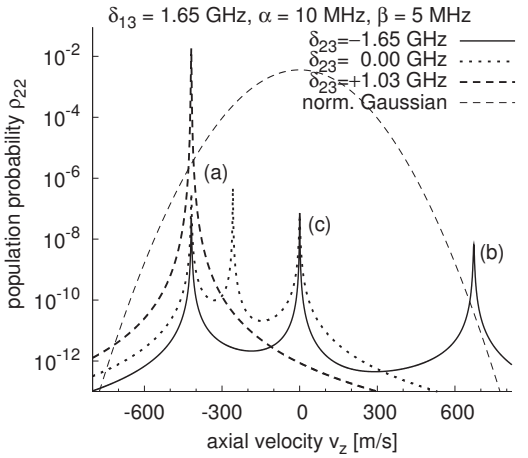


FIG. 2. Computed population probability of level $|2\rangle$. The detuning of the lower transition $\delta_{13}$ is fixed at +1.65 GHz. Three curves show $\rho_{22}$ as a function of the axial velocity $v_z$, each curve for a different detuning of the upper transition in the blue $\delta_{23}$. The (a)–(c) symbols on the curve for $\delta_{23}=-1.65$ GHz label the peaks for which a resonance condition is fulfilled. The thin dashed line shows the normalized Gaussian velocity distribution for room temperature.

$\Gamma_{21}=0.87/32.1$ ns$=(36.9$ ns$)^{-1}$, which describes population transfer by spontaneous emission from level $7\ ^1S_0$ to level $6\ ^1S_0$ (via $6\ ^1P_1$). The decay of the $7\ ^1S_0$ state to the $6\ ^3P_1$ state is given by $\Gamma_{31}=0.13/32.1$ ns$=(247$ ns$)^{-1}$.

The damping of the off-diagonal elements at line $|i\rangle$, column $|j\rangle$ in the density matrix is denoted by $\gamma_{ij}$. In general, the coherence $\tilde{\rho}_{ij}$ between two levels $|i\rangle$ and $|j\rangle$ is damped by half of the sum of the decay rates of both levels. Including damping caused by dephasing collisions between the atoms $\gamma_{ij_{\text{deph}}}$, the time constant of the off-diagonal elements is given by

$$\gamma_{31} = \frac{1}{2}\Gamma_{31} + \gamma_{31_{\text{deph}}},$$

$$\gamma_{23} = \frac{1}{2}(\Gamma_{21} + \Gamma_{23} + \Gamma_{31}) + \gamma_{23_{\text{deph}}},$$

$$\gamma_{21} = \frac{1}{2}(\Gamma_{21} + \Gamma_{23}) + \gamma_{21_{\text{deph}}}. \tag{2}$$

The collisional self-broadening for the $6\ ^1S_0-6\ ^3P_1$ transition in mercury at room temperature is $\gamma_{31_{\text{deph}}}=41$ kHz and $\gamma_{23_{\text{deph}}}=6$ kHz [15]. $\gamma_{21_{\text{deph}}}$ should be even smaller because dephasing collisions only occur between atoms that are connected via dipole transitions. As we excite the atomic mercury vapor with coherent continuous-wave laser beams and are not interested in relaxation, we set all time derivations in Eqs. (1a)–(1f) to zero. The whole population is always distributed among the three levels and cannot be lost. This yields the equation

$$\rho_{11} + \rho_{22} + \rho_{33} = 1. \tag{3}$$

Equations (1a)–(1f) and Eq. (3) as well as the complex conjugates of Eqs. (1d)–(1f) form a set of independent differential equations of first order [for $\dot{\rho}_{ii}=0$, Eq. (1b) is a linear combination of Eqs. (1a) and (1c)]. This system of equations is solved to obtain the populations $\rho_{ii}$ and coherences $\tilde{\rho}_{ij}$ as a function of the Rabi frequencies and detunings. The coherences are complex and include absorption (imaginary part) as well as dispersion (real part).

We now consider the motion of the atoms. We define the **z** axis to be parallel to the propagation direction of the laser beams. Due to the Doppler effect, a moving atom with a velocity component $v_z \neq 0$ will interact with detuned laser fields, $\delta_{13} \rightarrow \delta_{13}+k_{13}v_z$ and $\delta_{23} \rightarrow \delta_{23}+k_{23}v_z$ with $k_{ij}=\omega_{ij}/c$.

It is instructive to plot the population $\rho_{22}$ as a function of the atomic velocity $v_z$. This is shown in Fig. 2 for three different detunings $\delta_{23}$. The uv Rabi frequency is in the same order of magnitude as the decay rates. The three plots are all at the same uv detuning $\delta_{13}=1.65$ GHz; they differ only in $\delta_{23}$. For a detuning of the blue laser beam of $\delta_{23}=0$ GHz and $\delta_{23}=-1.65$ GHz three peaks appear in the spectrum. For the $\delta_{23}=-1.65$ GHz curve the three peaks are labeled (a)–(c). Peaks (a) and (b) are stepwise excitations [16], as the population in the upper level arises from a double one-photon excitation via the intermediate level. Peak (c) is a resonant two-photon transition directly from the ground to the upper state.

(a) This peak appears at the velocity

$$v_z = -2\pi\delta_{13}/k_{13}. \tag{4}$$

At this velocity the 254 nm laser beam is resonant with the lower transition $6\ ^1S_0-6\ ^3P_1$ resulting in a population maximum. This peak does not change its position for different detunings $\delta_{23}$ of the blue laser beam.

(b) This peak appears at the velocity

$$v_z = -2\pi\delta_{23}/k_{23}. \tag{5}$$

The 408 nm laser beam is resonant with the upper transition $6\ ^3P_1-7\ ^1S_0$ for atoms of this velocity. Atoms, which are

excited into the intermediate state $|3\rangle$ by an off-resonant laser field on the lower transition, are then resonant on the upper transition. The result is another maximum in population in the upper level. Peak (b) is similar to peak (a), just with the role of the two transitions interchanged.

(c) This peak appears at the specific velocity when atoms are resonant with the sum of both laser frequencies. If $\delta_{23}=-\delta_{13}$, for example, this peak appears at $v_z=0$, because the sum of the detunings exactly matches the level difference $6\ ^1S_0-7\ ^1S_0$. The condition which has to be fulfilled in this case is

$$v_z=-2\pi(\delta_{13}+\delta_{23})/(k_{13}+k_{23}), \tag{6}$$

the condition of the resonant two-photon transition.

For a continuous scan of $\delta_{23}$ from negative to positive values with $\delta_{13}$ fixed at 1.65 GHz, peaks (b) and (c) will shift toward negative abscissa values. The three curves in Fig. 2 are "snapshots" at the detunings $\delta_{23}=-1.65$, 0, and +1.03 GHz. The resonance condition of peak (a) does not depend on $\delta_{23}$ and stays at the same velocity $v_z$. At a specific detuning $\delta_{23}$, the three peaks (a), (b), and (c) overlap. In this case, both laser fields are resonant for one velocity class of atoms. Conditions (4)–(6) coincide in condition

$$\delta_{23}=\delta_{13}\frac{k_{13}}{k_{23}}. \tag{7}$$

This is the curve for $\delta_{23}=1.03$ GHz in Fig. 2. Note that the population in the upper level is several orders higher than the "single" peaks of the other curves. This is the basis of the velocity-selective double resonances.

The integration over all velocity classes gives the line shape, which is observed in the experiment. The Gaussian velocity distribution for mercury atoms at room temperature is shown in Fig. 2, too. For consecutive detunings $\delta_{23}$ the function $\rho_{22}(v_z)$ is multiplied with the Gaussian velocity distribution and integrated over $v_z$. This convolution has been done with numerical integration. During a frequency scan of the detuning $\delta_{23}$ peaks (b) and (c) are shifted through the center of the Gaussian velocity distribution. Consequently, two Doppler-broadened maxima will show up, one for the stepwise excitation (b) and one for the two-photon resonance condition (c). Additionally, a peak appears for the velocity-selective double resonance, which comes from the increased height of the coincidence of peaks discussed in case (c). This maximum is not Doppler broadened because only one velocity class contributes.

Figure 3 shows four plots of the population in the upper level $\rho_{22}$ versus the detuning on the upper transition $\delta_{23}$ computed for different Rabi frequencies. Note that the velocity-selective double resonance is only observable for low Rabi frequencies. Resonances occur at $\delta_{23}=-1.65$ GHz (two-photon resonance), 0 GHz (stepwise excitation with one-photon resonance), and 1.03 GHz (velocity-selective double resonance). The small shifts are due to the off-resonant uv laser causing asymmetry in the three-level system. The Doppler-broadened resonances are Voigt profiles of different widths. The natural linewidth in the velocity diagram (Fig. 2) is bigger for stepwise (b) than for two-photon (c) excitation

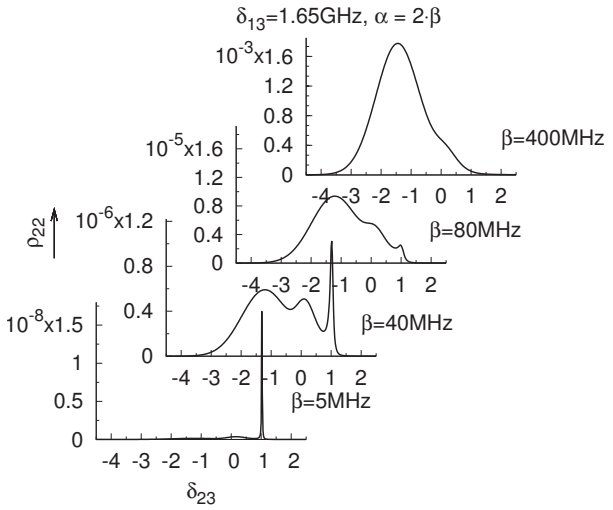


FIG. 3. Population probability of $|2\rangle$ versus the detuning $\delta_{23}$ shown for different Rabi frequencies $\alpha$ and $\beta$. Note the change of scale of the vertical axis. The detuning $\delta_{13}$ is fixed at +1.65 GHz, as before. For decreasing Rabi frequencies, the velocity-selective double resonance appears. This resonance dominates for very low $\alpha$ and $\beta$.

(two natural broadened levels participate in the stepwise excitation process, so the inverse decay rates add up), but the Doppler broadening of the two-photon resonance is about two times larger than that for the one-photon resonance (see Fig. 3). This can be seen from the conditions for both peaks in the velocity diagram (Fig. 2). The one-photon resonance obeys Eq. (5), with a proportionality factor $k_{13}^{-1}$ between $v_z$ and $\delta_{23}$, while for the two-photon resonance [Eq. (6)] this factor is $(k_{13}+k_{23})^{-1}$. Therefore, when scanning $\delta_{23}$, peak (c) shifts a factor of $k_{23}/(k_{13}+k_{23})$ less on the velocity axis than peak (b). This results in a 2.6-fold Doppler width of the two-photon resonance in the line shape after the convolution shown in Fig. 3.

The velocity-selective double resonance is due to the overlap of the three peaks in the velocity diagram ($\delta_{23}=1.03$ GHz) for one specific velocity class. Though this overlap is higher than the other single peaks, it is far away from the center of the Gaussian velocity distribution. To result in a significant resonance after the convolution, the peak height multiplied by the value of the Gaussian distribution for the same $v_z$ must be at least comparable to the height of peaks (b) and (c), multiplied with the maximum value of the Gaussian distribution at $v_z=0$. This is only the case for low Rabi frequencies as shown in Fig. 2.

Figure 4 shows the population of the upper level $\rho_{22}$ versus the velocity $v_z$ for the same detunings as in Fig. 2 but higher Rabi frequencies. Peaks (a) and (b) are saturation broadened due to the higher Rabi frequencies ($\alpha>\Gamma_{31}$ and $\beta>\Gamma_{23}$). The height of the overlap of the three peaks (for $\delta_{23}=1.03$ GHz) times the Gaussian is lower than the height of the single peaks (b) and (c) times the Gaussian. Therefore, the contribution of the velocity-selective double resonance to the total population $\rho_{22}$ after the convolution is negligible and cannot be observed in the upper graph in Fig. 3.

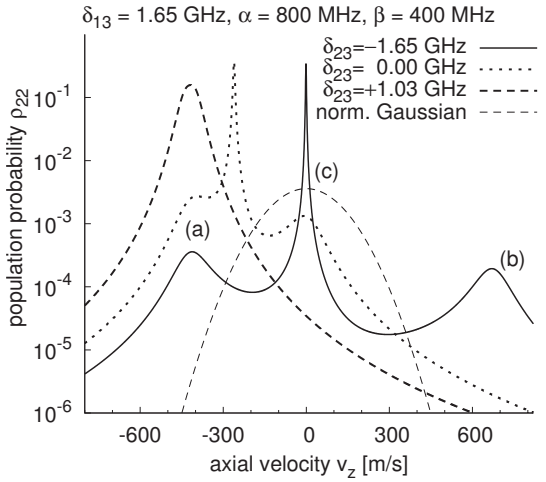


FIG. 4. Population of level $|2\rangle$ as a function of the axial velocity $v_z$. The detuning of the lower transition $\delta_{13}$ is kept fixed at 1.65 GHz. The Rabi frequencies (designated in the figure) are 80 times higher compared to Fig. 2.

## III. EXPERIMENTAL SETUP

A frequency-quadrupled solid-state disk laser with output powers of up to 750 mW at 254 nm [9] excites the lower transition $6\ ^1S_0-6\ ^3P_1$. The $6\ ^3P_1-7\ ^1S_0$ transition is driven by a frequency-doubled laser diode system with tapered amplifiers. This system gives up to 30 mW at 408 nm and can be detuned without mode hops about 20 GHz. Both laser beams have the same linear polarization. Cylindrical and spherical lenses are used to compensate for astigmatism and to match beam sizes. The beams are overlapped on a dichroic mirror and enter a mercury-filled fused silica cell of 5 mm length, where the interaction with the atoms takes place. The mercury vapor in our gas cell consists of a natural isotope mixture. In the calculation, we sum the contribution of the isotopes using the known shifts [17,18] with respect to a reference isotope, $^{202}$Hg, which is the most abundant [19]. The fluorescence out of the $7\ ^1S_0$ state at 1014 nm wavelength is detected by an InGaAs photodiode (Hamamatsu G8605-25). It is placed perpendicular to the beam propagation direction **z** to suppress stray light of the incident beams. The 408 nm beam is chopped and the signal is separated from the background by a lock-in amplifier. The fluorescence signal is proportional to the population of the $7\ ^1S_0$ level. We can thus compare the observed fluorescence to the calculation of the population $\rho_{22}$ in the upper level.

## IV. MEASUREMENTS

We recorded the fluorescence intensity as a function of the detuning of the 408 nm laser. All measurements presented here were performed at room temperature. We distinguish three cases for the uv detunings $\delta_{13}$ and the Rabi frequencies $\alpha$ and $\beta$: the far-resonant regime (Sec. IV A), the near-resonant regime (Sec. IV B), and the velocity-selective double resonances (Sec. IV C).

### A. Far-resonant regime

The far-resonant regime is characterized by a $\delta_{13}$, which is large enough to clearly separate the one-photon resonance from the two-photon resonance for all isotopes. The two-photon excitation is resonant if $\delta_{13}+\delta_{23}=0$. Figure 5 shows the measured fluorescence (dots) and the calculated population (solid line) of level $|2\rangle$, which is shown for the sum of all isotopes, as a function of $\delta_{23}$ for $\delta_{13}=-48$ GHz. Vertical bars show the position of the two-photon resonances for each isotope and the height of each bar represents the abundance of the isotope in the natural mixture. For larger detunings $\delta_{13}$, the shape of the two-photon resonance does not change. Only the height of the signal decreases, as the population in the upper level diminishes. To detect the two-photon resonance at larger detunings, both laser beams are focused to a 15 $\mu$m waist and a collection lens is used for the fluorescence detection.

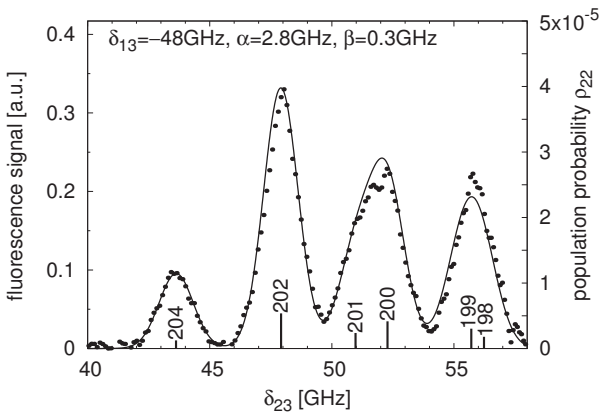


FIG. 5. Far-resonant regime. The dots display the measured fluorescence for $\delta_{13}=-48$ GHz and the solid line shows the computed curve for the sum of the populations of all isotopes. Vertical bars show the position and relative abundance of each isotope.

### B. Near-resonant regime

For small detunings $\delta_{13}$, two-photon and one-photon resonances of the various isotopes overlap. Accordingly, the resulting graph for the population of level $|2\rangle$ as a function of the detuning $\delta_{23}$ becomes more complex than in the far-resonant regime: the origin of each peak cannot be readily identified from looking at the graph. Perhaps the easiest way to identify the different peaks is to compare them with the calculation for separated isotopes. The isotope shifts in the $6\ ^3P_1$ level in the near-resonant regime can be larger than the detuning to each isotope's one-photon resonance $\delta_{13}$. Therefore, resonance peaks of less abundant isotopes can exceed resonances of more abundant isotopes if $\delta_{13}$ is in the vicinity of their one-photon resonance. Figure 6 shows the calculated (dashed) and experimental (dots) graph for a near-resonant case ($\delta_{13}=3.61$ GHz). Vertical bars indicate the position of the isotope's resonance, the type of resonance (solid: two-photon resonance; dashed: one-photon resonance), and their relative natural abundance (height of the bar). Two adjustments were necessary for the fit to the observed line shape: the collisional damping rate had to be set to $\gamma_{ij_{\mathrm{deph}}}=4$ MHz in Eq. (2), which is 100 times larger than the expected collision broadening. Foreign gas in the mercury cell might be

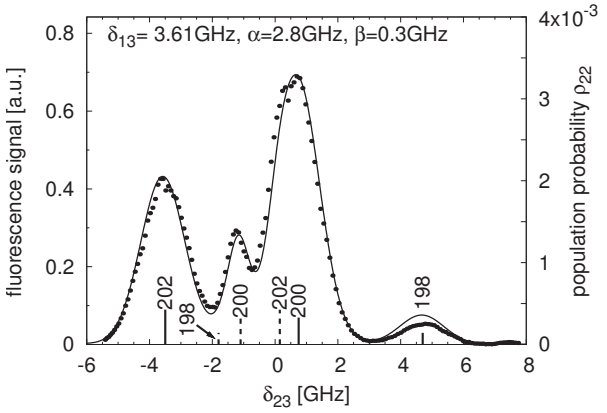


FIG. 6. Near-resonant case. The dots are the observed fluorescence for $\delta_{13}=3.61$ GHz and the dashed line is the calculated population of level $|2\rangle$. Other isotopes than those represented by vertical bars cannot be seen in this part of the spectrum.

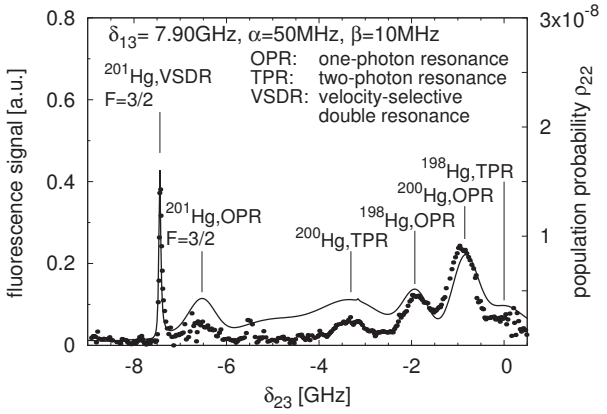


FIG. 7. Velocity-selective double resonance. The dots represent observed fluorescence for $\delta_{13}=7.90$ GHz and the dashed line is the calculated population $\rho_{22}$. The resonances from the isotopes and the different kinds of resonance for each isotope are marked in the graph. At $\delta_{23}\approx-7.4$ GHz a non-Doppler-broadened peak of the $^{201}$Hg isotope with total angular momentum $F=3/2$ appears. This is an experimental observation of the velocity-selective double resonance.

the reason for this additional broadening. This needs further investigation.

A second adjustment is the suppression of the two-photon resonance in the near-resonant case for odd isotopes. In the near-resonant case the hyperfine splitting of the odd isotopes can no longer be treated using different three-level systems but rather as a four-level ($^{199}$Hg) and five-level ($^{201}$Hg) system. The splitted intermediate level allows different excitation paths which can interfere destructively resulting in a suppressed two-photon resonance [3].

### C. Velocity-selective double resonance

The velocity-selective double resonance can only be observed for low Rabi frequencies and its population probability per atom is orders of magnitude lower; see Fig. 3. In the experiment, we therefore used large beams of about 2.5 mm diameter in order to interact with more atoms. Figure 7 shows the observed fluorescence as a function of the blue detuning for $\delta_{13}=7.90$ GHz. The velocity-selective double resonance is clearly visible.

Because of its velocity-selective nature, a non-Doppler-broadened line appears in the spectrum for condition (7) including the specific isotopic shifts, which is for $\delta_{13}=7.9$ GHz fulfilled for the $^{201}$Hg isotope with total angular momentum $F=3/2$ at $\delta_{23}\approx-7.4$ GHz. Velocity-selective double resonances of other isotopes are outside the scanning region or are, due to the small abundance ($^{196}$Hg) or the large one-photon detuning ($^{198}$Hg), too small to be distinguished.

This effect is similar to a well-known effect in $\Lambda$ systems, the so-called dark resonance, which occurs at the same condition [5]. For this velocity group, the two ground states are in a coherent superposition resulting in a suppressed one-photon excitation into the upper level. In the ladder system, the coherence of the upper and the ground level results in an enhanced two-photon transition but the one-photon transition to the intermediate level is suppressed. Therefore, spectroscopy of the intermediate level should result in a dark resonance just like in $\Lambda$ systems. The calculation of population of the intermediate level indeed shows a dip at the same condition.

## V. CONCLUSIONS

The two-photon resonance with the 7 $^1S_0$ level in atomic mercury has been investigated in detail. Line shapes have been calculated by convolving the solution of optical Bloch equations with the Doppler velocity distribution. In addition to resonant two-photon excitation and stepwise excitation a distinct velocity-selective double resonance has been observed. This is analogous to the dark resonance in $\Lambda$ systems. Experimentally, the fluorescence at 1014 nm has been observed as a function of blue detuning for a fixed uv detuning. At very low Rabi frequencies, we observed the velocity-selective double resonance.

## ACKNOWLEDGMENTS

We thank Professor P. E. Toschek for a stimulating discussion. We gratefully acknowledge support by the DFG and the BMBF.

[1] F. H. M. Faisal, R. Wallenstein, and R. Teets, J. Phys. B **13**, 2027 (1980).
[2] M. Niering *et al.*, Phys. Rev. Lett. **84**, 5496 (2000).
[3] J. E. Bjorkholm and P. F. Liao, Phys. Rev. Lett. **33**, 128 (1974).
[4] K.-J. Boller, A. Imamoglu, and S. E. Harris, Phys. Rev. Lett. **66**, 2593 (1991).
[5] G. Orriols, Nuovo Cim., B **53**, 1 (1979).

[6] I. Siemers, M. Schubert, R. Blatt, W. Neuhauser, and P. E. Toschek, Europhys. Lett. **18**, 139 (1992).
[7] A. Smith, W. Alford, and G. Hadley, J. Opt. Soc. Am. B **5**, 1503 (1988).
[8] M. Scheid, D. Kolbe, F. Markert, T. W. Hänsch, and J. Walz, Opt. Express **17**, 11274 (2009).
[9] M. Scheid, F. Markert, and J. Walz, Opt. Lett. **32**, 955 (2007).
[10] F. Markert, M. Scheid, D. Kolbe, and J. Walz, Opt. Express **15**, 14476 (2007).
[11] R. G. Brewer and E. L. Hahn, Phys. Rev. A **11**, 1641 (1975).
[12] J. A. Halstead and R. R. Reeves, J. Quant. Spectrosc. Radiat. Transf. **28**, 289 (1982).
[13] E. C. Benck, J. E. Lawler, and J. T. Dakin, J. Opt. Soc. Am. B **6**, 11 (1989).
[14] K. L. Menningen and J. E. Lawler, J. Appl. Phys. **88**, 3190 (2000).
[15] P. Laporte and H. Damany, J. Quant. Spectrosc. Radiat. Transf. **22**, 447 (1979).
[16] G. Grynberg and B. Cagnac, Rep. Prog. Phys. **40**, 791 (1977).
[17] S. Gerstenkorn, J. Labarthe, and J. Vergès, Phys. Scr. **15**, 173 (1977).
[18] W. Schweitzer, Jr., J. Opt. Soc. Am. **53**, 1055 (1963).
[19] M. G. Zadnik, S. Specht, and F. Begemann, Int. J. Mass Spectrom. Ion Process. **89**, 103 (1989).